RESEARCH ARTICLE

Evaluation of overpotentials on graphite and liquid Bi–Mg electrodes by current interruption

Kazuhiro Kumamoto[1] [ID] · **Akihiro Kishimoto[1]** · **Tetsuya Uda[1]**

Abstract

Our group proposes a new titanium smelting process via Bi–Ti alloy. This process is comprised of reduction of $TiCl_4$ by Bi–Mg liquid alloy, separation of Ti from Bi by distillation, and Mg electrolysis. In this study, the Mg electrolysis with Bi–Mg liquid alloy cathode was investigated. We firstly measured the IR-corrected polarization curves on graphite and Bi–Mg liquid alloys by the current interruption method. The results indicated that the Bi–Mg alloy cathode can reduce the electricity consumption of the Mg electrolysis. In addition, from the relaxation curves on graphite and Bi–Mg alloys, the concentration overpotential on the Bi–Mg alloy is mainly due to mass transfer of Mg from the electrode/molten salt interface to the liquid alloy bulk. At current densities higher than 300 mA cm^{-2}, Mg-rich solid phases such as Bi_2Mg_3 and/or pure solid Mg are assumed to be deposited on the Bi–Mg liquid alloy cathode. Finally, we estimated the electricity consumption of the Mg electrolysis in the new smelting process based on the measured overpotentials, assuming that Bi–Mg liquid alloy cathode is stirred sufficiently and a low current density, 275 mA cm^{-2}, is applied. Under these conditions, the total electricity consumption of the Mg electrolysis in the new process will be lower than that in the Kroll process when the anode–cathode distance is smaller than 8 cm.

✉ Kazuhiro Kumamoto
  kumamoto.kazuhiro.43v@st.kyoto-u.ac.jp

✉ Tetsuya Uda
  uda.tetsuya.5e@kyoto-u.ac.jp

1 Department of Materials Science and Engineering, Graduate School of Engineering, Kyoto University, Yoshidahonmachi, Sakyo-ku, Kyoto 606-8501, Japan

Graphic abstract

IR-corrected polarization curves of (a) Mg^{2+} reduction on graphite and Bi–Mg liquid alloys and (b) Cl_2 evolution on graphite in $MgCl_2$–NaCl–KCl at 550 °C were measured by the current interruption method, and electricity consumption of Mg electrolysis in the new Ti smelting process was estimated from these results.
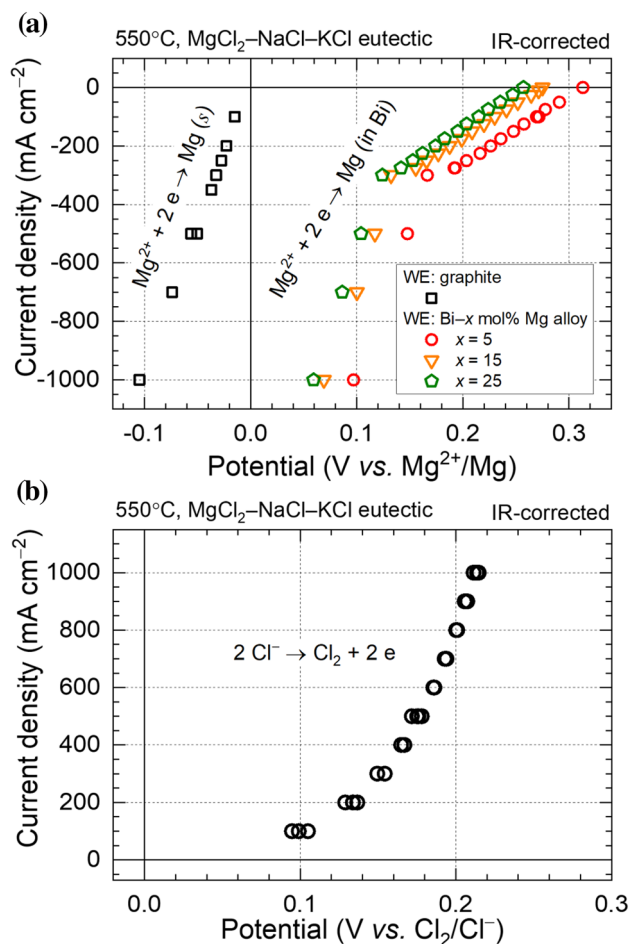

Keywords Molten salt · Overpotentials · Magnesium electrolysis · Bi–Mg alloy

1 Introduction

Titanium (Ti) is commercially produced by the Kroll process [1] in which titanium tetrachloride ($TiCl_4$) is reduced to porous Ti metal by magnesium (Mg). However, the productivity is low, and new smelting processes have been investigated, e.g., FFC-Cambridge process [2], OS process [3], Armstrong process [4], Subhalide reduction process [5], PRP [6], and HAMR process [7]. Our group proposes a new Ti smelting process via bismuth (Bi)–Ti liquid alloy [8–12]. Figure 1 is a schematic diagram of the new process for Ti. In the reduction cell, $TiCl_4$ is reduced by Bi–Mg alloy, and Bi–10 mol% Ti liquid alloy is produced at 900 °C. In the next segregation cell, the alloy is cooled to 500 °C, and a Ti-rich compound, Bi_9Ti_8, is precipitated in liquid Bi. Bi_9Ti_8

is then separated from liquid Bi and distilled to produce Ti powder in the distillation cell. Magnesium chloride ($MgCl_2$), a by-product in the reduction cell, is electrolyzed to produce Mg and chlorine gas (Cl_2) with a Bi–Mg liquid alloy cathode. The addition of Bi into the reduction cell makes it possible to transfer Ti in the liquid alloy state continuously. In addition, the feed rate of $TiCl_4$ can be improved because Bi also works as a coolant [9].

In the Kroll process, Mg and Cl_2 are produced by electrolysis of $MgCl_2$ with graphite cathode and anode. The reactions are described as follows:
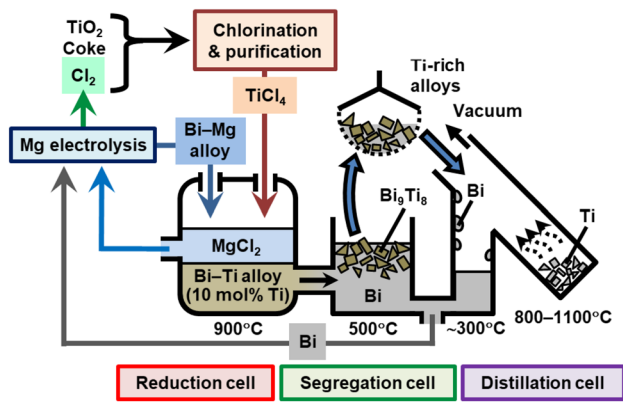
$$\text{Cathode: } Mg^{2+} + 2\,e \ \rightarrow \ Mg\,(l) \tag{1}$$

$$\text{Anode: } 2\,Cl^- \ \rightarrow \ Cl_2(g) + 2\,e \tag{2}$$
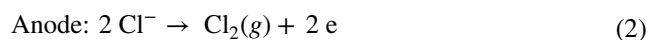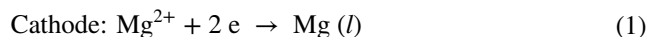
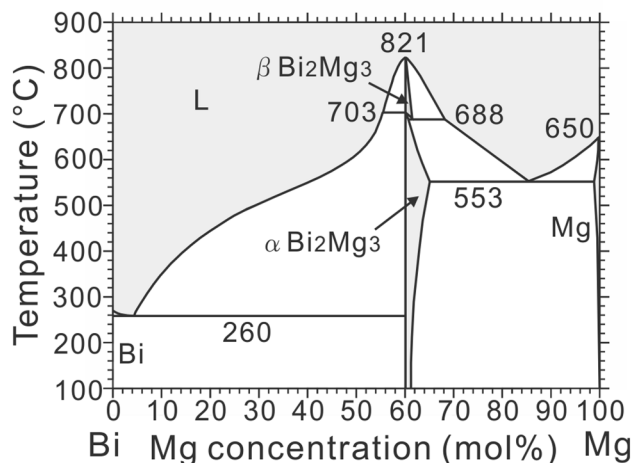**Fig. 1** Schematic of the proposed new smelting process
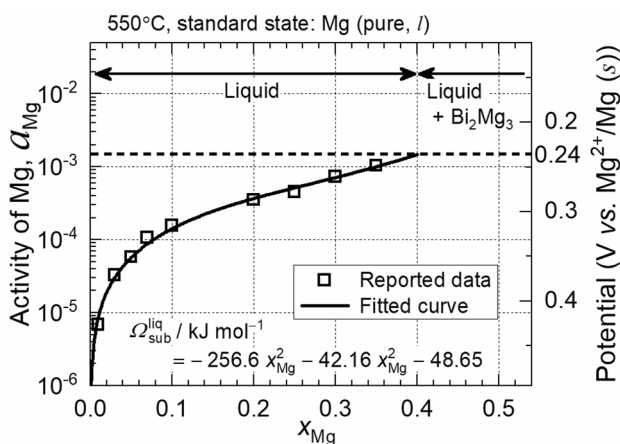

Fig. 3 Bi–Mg phase diagram [21]

Fig. 2 Reported activity of Mg in Bi–Mg alloy [20] and potential of Bi–Mg alloy versus Mg^{2+}/Mg (s) at 550 °C. Fitted curve is determined assuming a subregular solution model (interaction parameter, $\Omega_{sub}^{liq}/kJ\ mol^{-1} = -256.6\ x_{Mg}^2 - 42.16\ x_{Mg} - 48.65$ where x_{Mg} is the mole fraction of Mg in Bi–Mg alloy). The standard state of Mg is converted from solid to liquid by the Gibbs energy of melting of Mg at 550 °C, 907.6 J mol⁻¹ [35]

Because the Mg electrolysis accounts for 70–80% [13] of the total energy consumed in the Kroll process, it is quite important to improve the efficiency of Mg electrolysis. For this reason, many studies on Mg deposition in molten salts have been made [14–19]. In the new process, Bi–Mg liquid alloy is used as the cathode of Mg electrolysis, and Mg^{2+} ion is reduced at a liquid Bi cathode by the following reaction.

Cathode: $Mg^{2+} + 2\,e \rightarrow Mg$ (in Bi) (3)
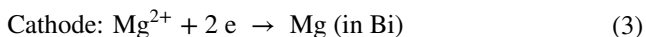
The liquid Bi cathode may reduce the electricity consumption of the Mg electrolysis due to the small activity coefficient of Mg in Bi. For example, the activity coefficient of Mg is 1.81×10^{-3} in Bi–25 mol% Mg alloy at 550 °C [20]. Figure 2 shows the activity of Mg in Bi–Mg alloy and corresponding oxidation–reduction potential of Mg in the alloy

relative to pure liquid Mg. Considering the small activity of Mg in the alloy, the decomposition voltage of $MgCl_2$ is reduced by 12% in comparison with that of the Mg electrolysis. The calculation of the decomposition voltage is described in Appendix. The Bi–Mg alloy can be directly used for the reduction of $TiCl_4$ in the reduction cell. In addition, Bi-rich Bi–Mg alloys have lower melting points than pure Mg as seen in Fig. 3 [21]. Thus, the electrolysis can be operated at a lower temperature than that of the Mg electrolysis in the Kroll process, which prolongs the lifetime of the electrolytic cell. Furthermore, the liquid Bi cathode may improve the current efficiency of the electrolysis. In the electrolytic cell of the Kroll process, liquid Mg droplets move upward with Cl_2 gas bubbles in the flowing electrolyte. Then, it is reported that a back reaction, recombination of Mg and Cl_2, occurs and decreases the current efficiency [22]. Since the density of Bi is much higher than that of electrolyte, Bi–Mg alloy can be easily separated from Cl_2 bubbles.

Liquid alloy electrodes, such as Mg–lead (Pb) alloy cathode for Mg electrolysis [23, 24] and Mg–antimony (Sb) alloy electrode for liquid metal batteries [25, 26], were investigated. However, the electrochemical behavior of Bi–Mg alloy electrode has not been researched sufficiently. In the present study, the overpotentials on graphite anode and Bi–Mg alloy cathode were measured by the current interruption method, and the electricity consumption of the Mg electrolysis in the new process was estimated.

2 Experimental

2.1 Preparation of electrolyte and electrodes

$MgCl_2$ (97%, Wako Pure Chemical Industries, Ltd.), NaCl (99.5%, Nakalai Tesque, Inc.), and KCl (99.5%,

Nakalai Tesque, Inc.) were mixed in a glove box with argon (Ar) atmosphere at the eutectic composition of $MgCl_2$:NaCl:KCl = 50:30:20/mol% (m.p. 396 °C [27]). The mixed salt was dried under vacuum at higher temperatures than 226 °C for more than 54 h. The salt was filled in a nickel (Ni) crucible (OD 8.2 cm × ID 7.8 cm) and heated to 550 °C under Ar gas flow. After the salt was melted, pre-electrolysis with graphite anode and cathode was carried out at a cell voltage of 1.2–1.3 V. Before pre-electrolysis, small anodic and cathodic peaks were confirmed between 1.1 and 1.7 V versus Mg^{2+}/Mg in cyclic voltammogram. These peaks could be attributed to reaction of impurities derived from water. After the pre-electrolysis for 10 h, the residue current became smaller than 1 mA cm^{-2}. In the present study, Mg was electrochemically deposited on a Mo wire in the molten salt and used as reference electrode (RE). It was confirmed that the potential difference between Mg deposited on the Mo wire and pure Mg plate was smaller than 1.5 mV for more than 100 min.

Figure 4 shows the experimental apparatus. Bi–Mg alloy electrodes were prepared from pure Bi shot (99.999%, Kamioka Mining & Smelting Co., Ltd.). A magnesia (MgO) crucible (OD 1.4 cm × ID 1.0 cm, 99.6%, Nikkato Co., Ltd.) was fixed to a stainless steel tube (S. S. tube) as shown in Fig. 4. About 6 g of Bi shot was put into the MgO crucible, and Mo wire covered by a MgO tube (OD 2 mm × ID 1 mm, 99.6%, Nikkato Co., Ltd.) was inserted into the Bi shot as an electrical lead. After the Bi electrode was immersed into the molten salt, Bi–x mol% Mg alloy electrodes (x = 5, 10, 15, 20, and 25) were prepared by cathodic Mg deposition and anodic Mg dissolution on the molten Bi. The concentrations of Mg in the alloys were controlled by the electrical charge of the electrolysis. After all the electrochemical measurements, the Bi–25 mol% Mg alloy electrode was analyzed by energy-dispersion X-ray spectroscopy (EDX, JXA-8530F, JEOL Ltd.) and inductively coupled plasma atomic emission spectroscopy (ICP-AES, SPS3520UV, SII Nano Technology Inc.). Other metals such as sodium and potassium
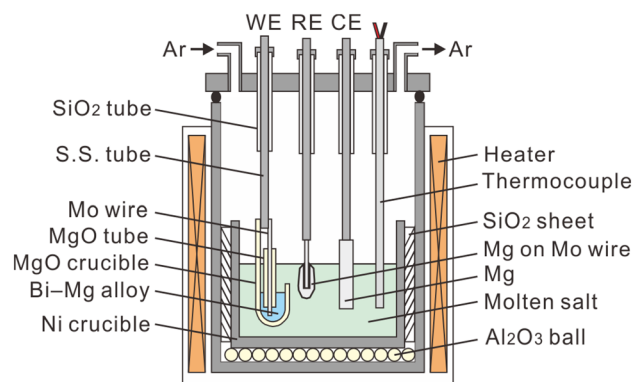

Fig. 4 Apparatus for electrochemical measurements

were not detected in the alloy from the results of EDX, and the concentration of Mg was confirmed to be 25.1 mol% by ICP-AES.

2.2 Current interruption measurement

The current interruption method was used to measure the overpotential of Cl_2 evolution and Mg deposition. The counter electrode (CE) was a pure Mg plate or a graphite plate, and Mg deposited on Mo wire was used as RE. Galvanostatic electrolysis at various current densities was carried out for 2 or 250 s with a potentiogalvanostat (Solartron 1287, Solartron Analysis), and current interruption was carried out. After the constant current was interrupted, the relaxation of potential of working electrode (WE) versus RE was recorded with a high-speed data recorder (USB-6251 or USB-6341, National Instruments) at a sampling rate of 1.25×10^6 or 2×10^6 Hz until 2.0 ms just after the current interruption. From 0.05 to 600 s, the potential of WE versus RE was also recorded with a data recorder (Agilent 34972A, Agilent Technologies) at a sampling rate of 10 or 20 Hz. After 2 s electrolysis, the potential of the Bi–Mg alloy easily relaxed to the initial potential because of little change in the Mg concentration in the alloy. Thus, the next measurement was carried out immediately. In contrast, the change was not small at 250 s electrolysis. Thus, Mg in the Bi–Mg alloy was anodically dissolved before the next measurement. The same current interruption measurement was carried out for pure solid Mg deposition and Cl_2 evolution on a graphite rod electrode. Mg deposited on the graphite electrode was completely dissolved by applying an anodic potential before the next measurement.

3 Results

3.1 Cl_2 evolution on graphite

Figure 5 shows relaxation curves on the graphite electrode where the evolution of Cl_2 occurs by reaction (2). In Fig. 5, the time of the last data point before the current interruption is defined as 0 s. During the galvanostatic electrolysis (time, $t \leq 0$), the potential of WE versus RE is represented as:

$$\phi_{WE}(I \neq 0, t \leq 0) - \phi_{RE} = \Delta E_{eq} + \eta_r + \eta_c + V_{IR} \quad (4)$$

where ϕ_{WE} ($I \neq 0, t \leq 0$) is the potential of WE during electrolysis, ϕ_{RE} is the potential of RE, η_r is the reaction overpotential, η_c is the concentration overpotential, and V_{IR} is the IR drop due to the ohmic resistance of the electrolyte, assuming the resistance of metallic parts is negligible. ΔE_{eq} is the difference between the electrode potentials of WE and RE where the following reactions (5) and (6) are assumed to be at equilibrium, respectively.
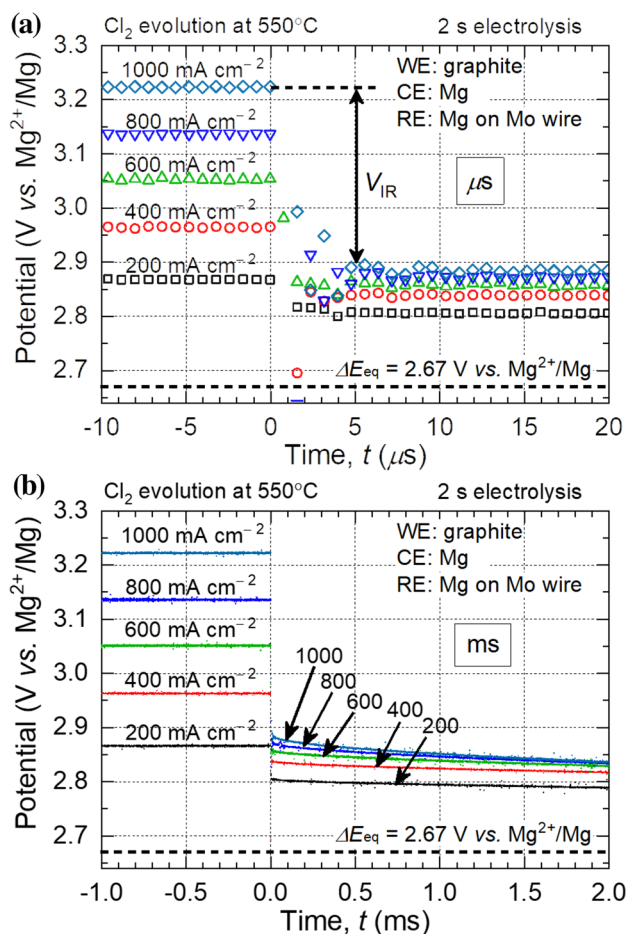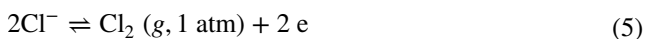
(a) Cl$_2$ evolution at 550°C — 2 s electrolysis

WE: graphite
CE: Mg
RE: Mg on Mo wire

ΔE_{eq} = 2.67 V vs. Mg^{2+}/Mg

(b) Cl$_2$ evolution at 550°C — 2 s electrolysis

WE: graphite
CE: Mg
RE: Mg on Mo wire

ΔE_{eq} = 2.67 V vs. Mg^{2+}/Mg

Fig. 5 Relaxation curves on graphite in MgCl$_2$–NaCl–KCl eutectic electrolyte in **a** μs time range, **b** ms time range
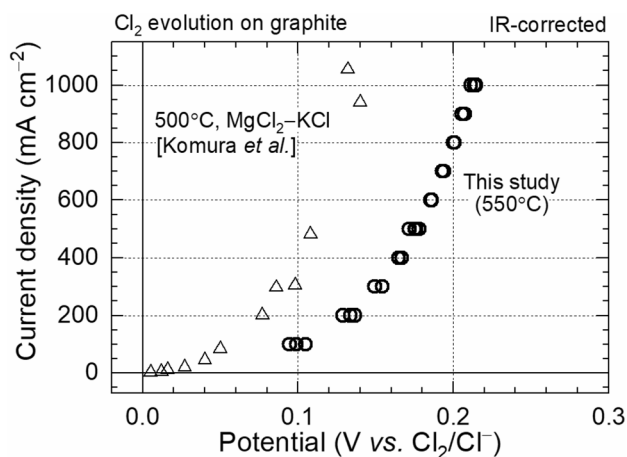

Fig. 6 IR-corrected polarization curves of Cl$_2$ evolution on graphite. Open circles denote data in the present study at 550 °C. The electrode potential of Cl$_2$/Cl$^-$ was calculated to be 2.67 V versus Mg^{2+}/Mg from the reported thermodynamic data (see Appendix). Open triangles denote the reported polarization behavior at steady-state in MgCl$_2$–KCl at 500 °C [28]. The concentration of MgCl$_2$ in the literature is unknown but is assumed to be between 28 and 58 mol% from the MgCl$_2$–KCl phase diagram [36]

$$2Cl^- \rightleftharpoons Cl_2\ (g,\ 1\ atm) + 2\ e \tag{5}$$

$$Mg^{2+} + 2\ e \rightleftharpoons Mg\ (s) \tag{6}$$

In this case, ΔE_{eq} is equal to the decomposition voltage of MgCl$_2$ in eutectic MgCl$_2$–NaCl–KCl. The activity of MgCl$_2$ in the present molten salt at 550 °C is calculated to be 0.182 (standard state: pure liquid Mg) with a subregular solution model and the reported thermodynamic data, and the corresponding decomposition voltage is 2.67 V (see Appendix). As seen in Fig. 5a, unexpected oscillation of the potential was observed for 5 μs after the current interruption. This unexpected oscillation will be attributed to the instruments or inductance of lead wires, and we did not use the initial 5 μs data for analysis. The IR drop, V_{IR}, immediately becomes zero at the current interruption measurements. Obvious relaxation is not observed from 5 to 20 μs, and the relaxation of the reaction and concentration overpotentials are assumed to be much slower than 20 μs. We can

therefore take the average of the data points from 5 to 20 μs as $\Delta E_{eq} + \eta_r + \eta_c$. Figure 6 shows the IR-corrected polarization curve of Cl$_2$ evolution on the graphite. As the data are already IR-corrected, the potential corresponds to the overpotential. The current density increases exponentially with overpotential. The behavior in this study is similar to the reported polarization curve at 500 °C [28]. Moreover, the overpotential in this study is larger than the reported values. If we assume that the small temperature difference and the concentration difference in the molten salts do not affect, the reasons are probably attributed to difference in roughness of graphite electrode surface, coverage ratio of the electrode by Cl$_2$ bubbles on electrode, and so on.

3.2 Mg^{2+} reduction on Bi–Mg alloy

Figures 7 and 8 show the relaxation curves on the Bi–Mg alloy after 2 s and 250 s electrolysis, respectively. On the Bi–Mg alloy electrode, reaction (3) is expected to occur. The sum of the overpotentials was determined in the same way as for the graphite electrode. ΔE_{eq} in Eq. (4) was determined by the open circuit potential of the Bi–Mg alloy before the electrolysis. Figures 7c and 8c show that the potential relaxes slowly and there is a plateau region after electrolysis at current densities higher than 300 mA cm^{-2}.
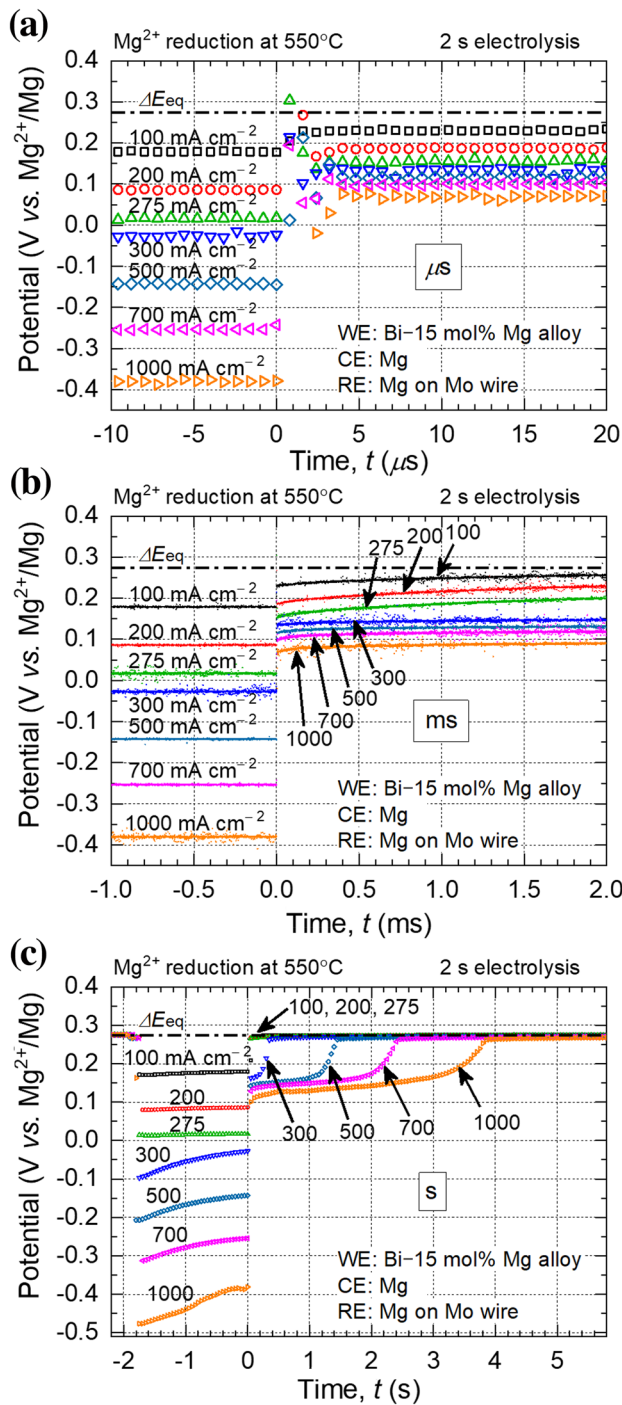
Fig. 7 Relaxation curves on Bi–15 mol% Mg alloy after 2 s electrolysis in MgCl$_2$–NaCl–KCl eutectic electrolyte in **a** μs time range, **b** ms time range, **c** s time range. The last data point before the current interruption is defined as 0 s

Fig. 8 Relaxation curves on Bi–5 mol% Mg alloy after 250 s electrolysis in MgCl$_2$–NaCl–KCl eutectic electrolyte in **a** μs time range, **b** ms time range, **c** s time range. The last data point before the current interruption is defined as 0 s

Fig. 9 Relaxation curves on graphite after 2 s electrolysis in MgCl$_2$–NaCl–KCl eutectic electrolyte in **a** μs time range, **b** ms time range, **c** s time range. The last data point before the current interruption is defined as 0 s
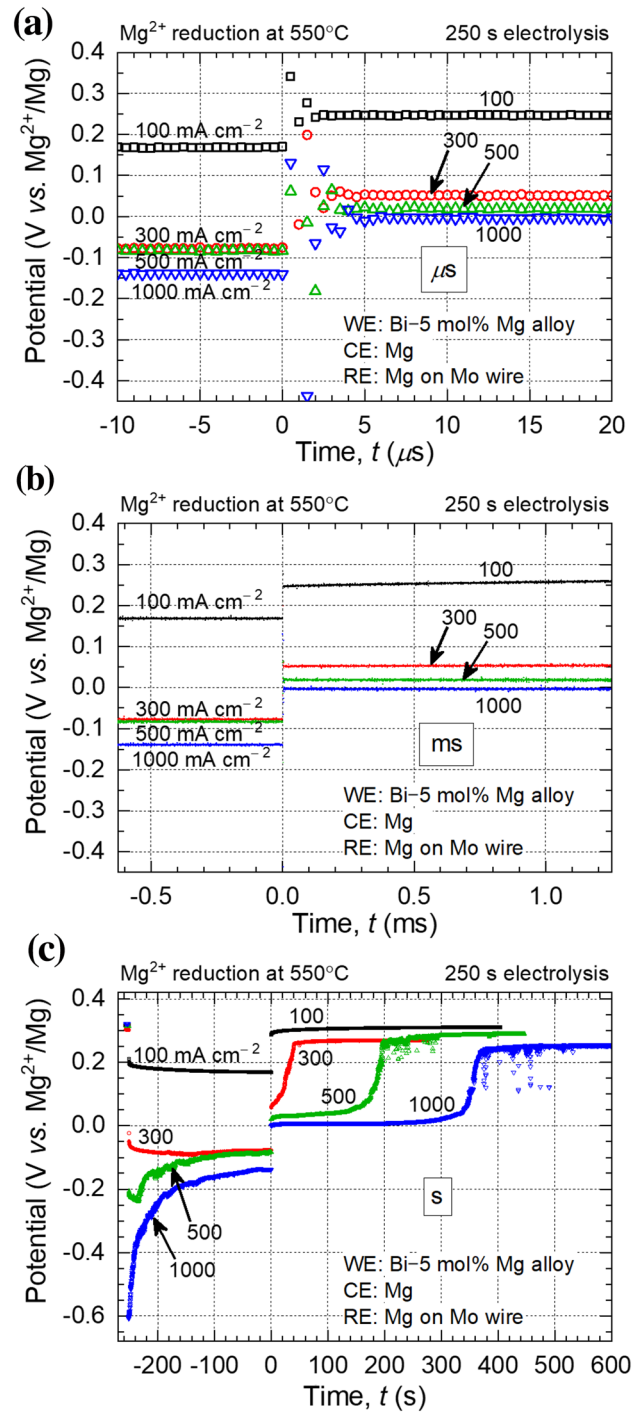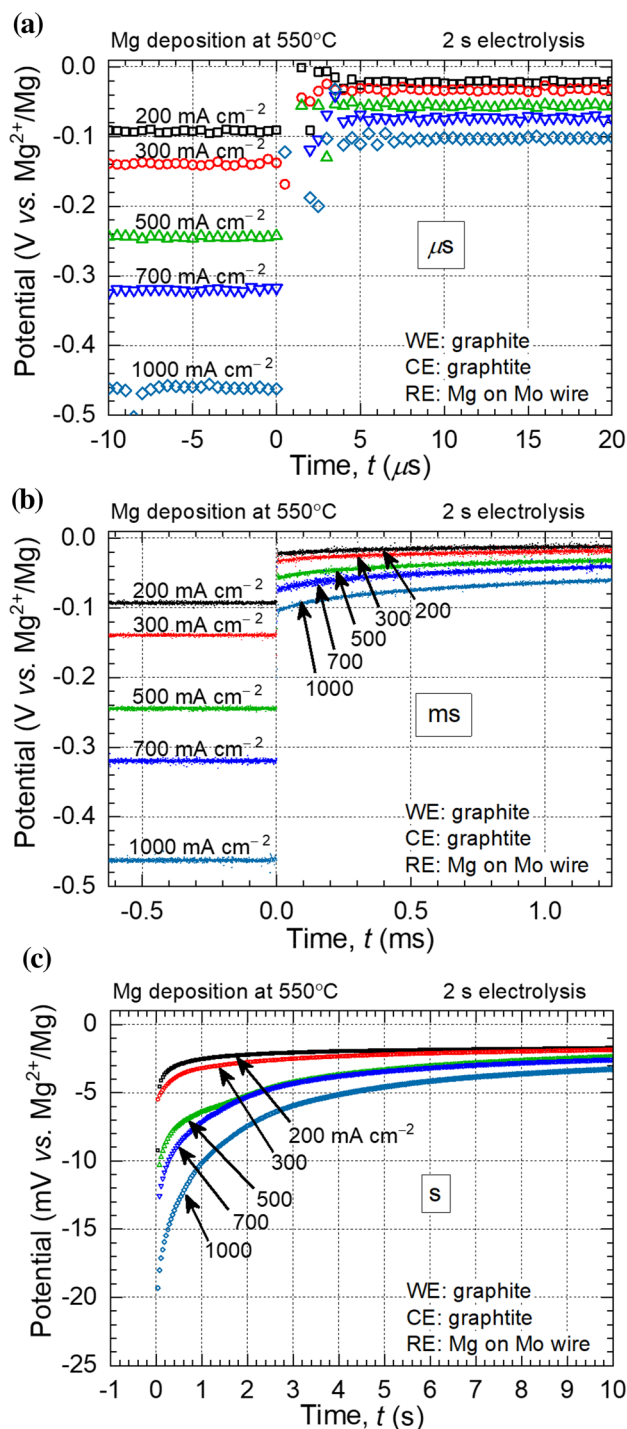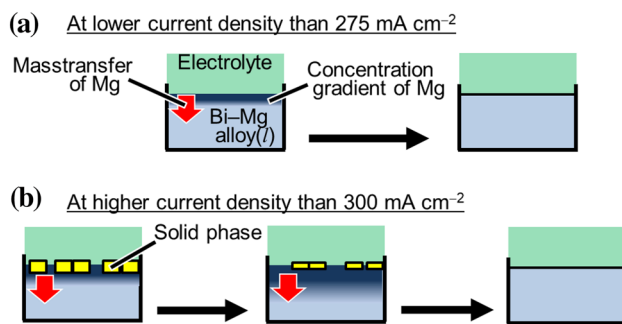

Fig. 10 Schematic of Mg concentration in Bi–Mg alloy after electrolysis

4 Discussion

4.1 The concentration overpotentials on Bi–Mg alloy

We don't have the data between 2.0 ms and 0.05 s after the current interruption. However, the plateau region suggests that the relaxation of the reaction overpotential completes in 0.1 s after the current interruption, and the slow relaxation after 0.1 s should be attributed to the concentration overpotential. On the Bi–Mg alloy, the concentration overpotential consists of two parts and is represented as:

$$\eta_c = \eta_c^{electrolyte} + \eta_c^{alloy} \tag{7}$$

where $\eta_c^{electrolyte}$ is the concentration overpotential caused by mass transfer of Mg^{2+} in the electrolyte, and η_c^{alloy} is caused by mass transfer of Mg from the electrode/molten salt interface to the liquid alloy bulk.

As a simple case, Mg deposition on a graphite rod electrode was investigated. The relaxation curves on graphite after 2 s electrolysis are shown in Fig. 9. In Fig. 9c, no plateau was observed on the relaxation curves on graphite. In addition, the concentration overpotential on graphite were much smaller than those on Bi–Mg alloy shown in Fig. 7c. For example, the values at 0.1 s on graphite and Bi–Mg alloy were about − 17 mV and − 164 mV at 1000 mA cm^{-2}, respectively. If the concentration overpotential in the electrolyte on Bi–Mg alloy, $\eta_c^{electrolyte}$, behaves in the same way as the concentration overpotential on graphite, the large overpotential on Bi–Mg alloy is not due to the concentration overpotential in electrolyte, but mainly due to the concentration overpotential in the alloy, η_c^{alloy}. The slow relaxation after 250 s electrolysis in Fig. 8c is also considered to be due to the concentration overpotential in the alloy. Considering the
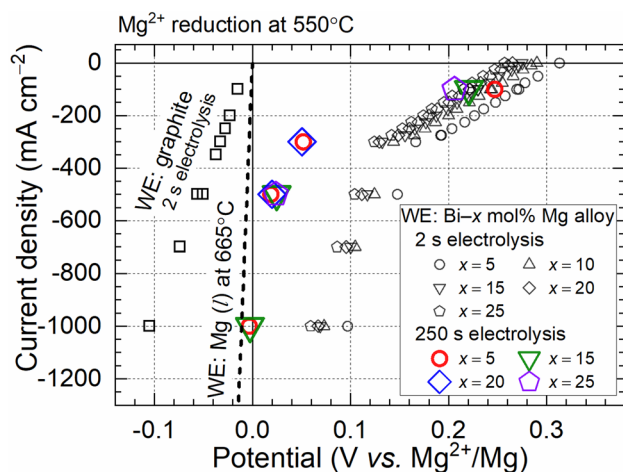
Fig. 11 IR-corrected polarization curves on Bi–Mg alloy and graphite in MgCl$_2$–NaCl–KCl eutectic electrolyte at 550 °C. Dashed line is the IR-free polarization curve of Mg (l) deposition on Mg (l) electrode in MgCl$_2$–NaCl equimolar electrolyte at 665 °C calculated using the Butler-Volmer equation of the symmetry coefficient is 0.5 and reported exchange current density of 3.65 A cm^{-2} [17]
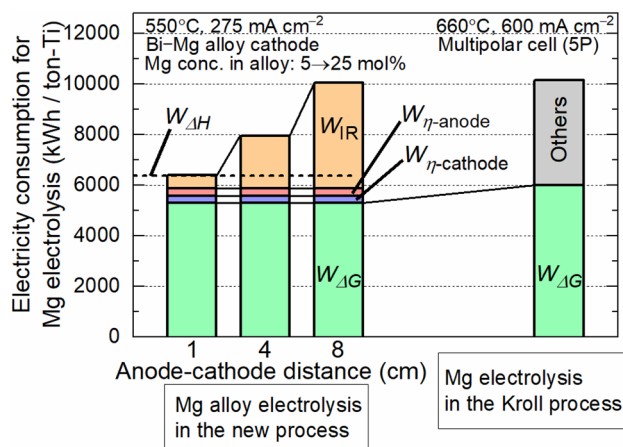

Fig. 12 Estimated electricity consumption of Mg electrolysis. $W_{\Delta G}$ is the theoretical electricity consumption. $W_{\eta\text{-anode}}$ and $W_{\eta\text{-cathode}}$ are the electricity consumed by overpotentials on the anode and cathode, respectively. W_{IR} is the electricity consumed by the IR drop attributed to the electrolyte. $W_{\Delta H}$ is the enthalpy change of the cell reaction of the Mg electrolysis

activity of Mg in Bi–Mg alloy shown in Fig. 2, the potential of liquid Bi–Mg alloy is more positive than 0.24 V versus Mg^{2+}/Mg. At current densities higher than 300 mA cm^{-2}, each relaxation curve shows a plateau at a more negative potential than 0.24 V as shown in Figs. 7c and 8c. Therefore, Mg-rich solid phases such as Bi$_2$Mg$_3$ and pure Mg were probably deposited on the surface of Bi–Mg alloy at current densities higher than 300 mA cm^{-2}. This situation is schematically illustrated in Fig. 10. At current densities lower than 275 mA cm^{-2}, the Bi–Mg alloy should be in a single liquid phase as shown in Fig. 10a. After the electrolysis, the potential relaxes as the concentration gradient of Mg decreases by the convection and the diffusion in the liquid alloy. In contrast, at current densities higher than 300 mA cm^{-2}, solid phases are deposited on the surface as shown in Fig. 10b. The Mg concentration in the liquid phase at the surface does not change until the solid phases disappear. Thus, the solid phases make the relaxation of potential slower.

4.2 Polarization curves on Bi–Mg alloy and graphite

The IR-corrected polarization curves on Bi–Mg alloy and graphite are shown in Fig. 11. From Fig. 11, the reduction of Mg^{2+} on Bi–Mg alloy starts at more positive potentials than that on graphite. This result indicates that the electricity consumption of Mg electrolysis can be reduced by Bi–Mg alloy. However, in a prolonged electrolysis at higher current densities than 300 mA cm^{-2}, the overpotential on Bi–Mg alloy becomes so large that the potential becomes almost 0 V versus Mg^{2+}/Mg. In this situation, solid phases may form at the interface. Thus, to reduce electricity consumption, it is

important to keep the concentration overpotential small by stirring the alloy or applying a low current density.

In Fig. 11, the dashed line is a polarization curve of molten Mg deposition on molten Mg electrode in MgCl$_2$–NaCl equimolar electrolyte at 665 °C in literature [17]. There is a large difference between the values in the literature and the present study. We do not consider that the small temperature difference and the different state of deposited Mg between liquid and solid can account for this difference. The difference of electrolysis time, about 0.1 ms in the literature [16] and 2 s in this study, might have affected the results.

4.3 Estimation of the industrial electricity consumption

We can estimate the electricity consumption of Mg electrolysis using the data obtained in this study. Figure 12 shows the results of estimation. The operating temperature in the new process is tentatively fixed at 550 °C. Inlet and outlet Mg concentrations in alloy are assumed to be 5 and 25 mol%, respectively. Theoretical electricity consumption, $W_{\Delta G}$, and the enthalpy change of the cell reaction, $W_{\Delta H}$, are calculated from the reported thermodynamic data as shown in Appendix. The current density is set at 275 mA cm^{-2}, above which solid phases would form on the alloy cathode. The values of the overpotentials obtained in the 2 s electrolysis experiment are used in this estimation, assuming that the same concentration overpotential would be achieved in industrial operation by stirring the alloy. The electricity consumed by the IR drop due to the electrolyte, W_{IR}, is estimated from the reported conductivity of MgCl$_2$–NaCl–KCl eutectic electrolyte, 1.18 S cm^{-1}, at 475 °C [29]. The current efficiency is

assumed to be 100%. As for the Mg electrolysis in the Kroll process, the reported operation temperature and current density are 660 °C [22] and 600 mA cm^{-2} [13], respectively. The total electricity consumption is reported to be 10155 kWh/ton-Ti [13], and the theoretical electricity consumption, $W_{\Delta G}$, is calculated from thermodynamic data. From Fig. 12, when the anode–cathode distance is smaller than 8 cm in the new process, the total electricity consumption will be lower than that in the Kroll process. For isothermal operation at 550 °C without heat supply to the electrolytic cell, the total energy cannot be lower than $W_{\Delta H}$. Therefore, the anode–cathode distance in the new process should be larger than 1 cm. We also have to consider heat dissipation from the bath in industrial electrolysis, so a longer distance is appropriate.

5 Conclusions

In this study, the IR-corrected polarization curves on graphite and Bi–Mg liquid alloy are obtained by the current interruption method. At current densities higher than 300 mA cm^{-2}, solid phases such as Bi_2Mg_3 and/or pure solid Mg are expected to be deposited on the Bi–Mg alloy cathode. It is found that the concentration overpotential on the Bi–Mg alloy is mainly due to mass transfer of Mg from the electrode/molten salt interface to the liquid bulk. Consequently, stirring the Bi–Mg alloy is needed for electrolysis with smaller overpotentials. We then estimated the electricity consumption of the Mg electrolysis in the new smelting process based on the measured overpotentials, assuming sufficient stirring of alloy cathode and a low current density. The total electricity consumption of the Mg electrolysis in the new process will be lower than that in the Kroll process when the anode–cathode distance is smaller than 8 cm.

Appendix 1

Calculation of the theoretical electricity consumption of Mg electrolysis

Data used for the thermodynamic calculation are given in Table 1. The activities of $MgCl_2$ in Table 1 are calculated by a subregular solution model, in which the excess molar Gibbs energy of ternary molten salt, G^{ex}, is represented as Eq. (8).

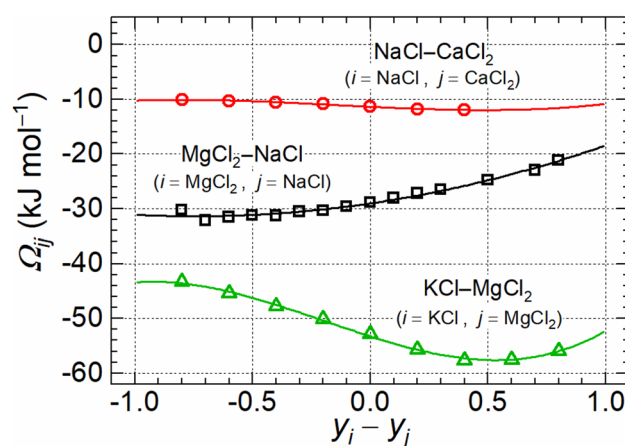$$G^{ex} = \Omega_{12}x_1x_2 + \Omega_{23}x_2x_3 + \Omega_{31}x_3x_1 \tag{8}$$

Fig. 13 Interaction parameters of $MgCl_2$–NaCl, NaCl–$CaCl_2$, and KCl–$MgCl_2$ molten salts calculated from the reported data. Solid lines are fitted curves by Eq. (11)

Table 1 Data used for the calculation of theoretical electricity consumption of the Mg electrolysis in the Kroll process and the new process

	Kroll process	New process
Operating temperature (°C)	660 [22]	550
Composition of molten salt	$MgCl_2$:NaCl:$CaCl_2$ = 16:64:20/mol% [14]	$MgCl_2$:NaCl:KCl = 50:30:20/mol%
The standard Gibbs energy of formation of $MgCl_2$ (kJ mol^{-1})^a	− 491	− 503
Activity of $MgCl_2$	2.61×10^{-2}	1.82×10^{-1}
Activity of Mg	1	$5.69 \times 10^{-5} - 5.16 \times 10^{-4b}$ ($x_{Mg} = 0.05 - 0.25$)
Decomposition voltage (V)	2.69	$2.32 - 2.40^c$ ($x_{Mg} = 0.05 - 0.25$)
Theoretical electricity consumption (kWh/ton-Ti)	6030	5310

^{a}Reported data [37] are interpolated to the operating temperature. The standard states of Mg and $MgCl_2$ both are pure liquid

^{b}Calculated by a subregular solution model with a interaction parameter, Ω_{sub}^{liq}/kJ mol$^{-1} = -256.6x_{Mg}^2 - 42.16x_{Mg} - 48.65$ where x_{Mg} is the mole fraction of Mg in Bi–Mg alloy

^{c}When the activity of Mg is unity, the decomposition voltage is 2.67 V

Table 2 Parameters used for the calculation

Process/components	(i, j)	Parameter in Eq. (11) (kJ mol^{-1})				References
		L_0^{ij}	L_1^{ij}	L_2^{ij}	L_3^{ij}	
Kroll process	(1, 2)	− 29.0	6.32	4.25	–	[30]
1 = MgCl$_2$	(2, 3)	− 11.3	− 2.07	0.823	1.78	[30]
2 = NaCl	(3, 1)	3.68	− 4.83	1.36	–	[32]
3 = CaCl$_2$						
New process	(1, 2)	− 29.0	6.32	4.25	–	[30]
1 = MgCl$_2$	(2, 3)	− 2.19	− 0.136	–	–	[33]
2 = NaCl	(3, 1)	− 53.3	− 13.7	5.43	9.28	[30]
3 = KCl						

In Eq. (8), x_1, x_2, and x_3 are the mole fractions of components 1, 2, and 3 in the ternary molten salts, respectively, and Ω_{ij} are interaction parameters of binary molten salts composed of i and j. The compositions of the molten salts are shown in Table 1. We defined the components 1 and 2 as MgCl$_2$ and NaCl, respectively. The component 3 is defined as CaCl$_2$ or KCl in the Kroll process or new process, respectively. The activity coefficient of MgCl$_2$, γ_1, can be calculated from the following equation.

$$RT\ln\gamma_1 = G^{\text{ex}} - x_2\left(\frac{\partial G^{\text{ex}}}{\partial x_2}\right)_{P,T,x_3} - x_3\left(\frac{\partial G^{\text{ex}}}{\partial x_3}\right)_{P,T,x_2} \quad (9)$$

In Eq. (9), R is the gas constant, T is the absolute temperature, P is the pressure. Then, interaction parameters of the binary salts, Ω_{ij}, are collected as below.

For MgCl$_2$–NaCl, NaCl–CaCl$_2$, and KCl–MgCl$_2$ binary salts, data points of excess molar Gibbs energies for binary salts, G_{ij}^{ex}, are reported in literature [30]. Then, Ω_{ij} are obtained by Eq. (10) and fitted by Eq. (11) which is a Redlich–Kister polynomial [31].

$$\Omega_{ij} = \frac{G_{ij}^{\text{ex}}}{y_i y_j} \quad (10)$$

$$\Omega_{ij} = \sum_{n=0}^{m} L_n^{ij}\left(y_i - y_j\right)^n \quad (m \leq 3) \quad (11)$$

In Eqs. (10) and (11), y_i and y_j are mole fractions of i and j in the binary salts, and L_n^{ij} should be function of temperature. However, we assumed that L_n^{ij} are independent of temperature and adopted the data above 700 °C. Then, Ω_{ij} are function of the mole fractions. Figure 13 shows Ω_{ij} versus $y_i - y_j$ and fitted curves by Eq. (11). The fitting parameters, L_n^{ij}, are shown in Table 2. As for CaCl$_2$–MgCl$_2$ [32] and NaCl–KCl [33] molten salts, interaction parameters are reported as Eqs. (12) and (13), respectively.

$$\text{CaCl}_2\text{–MgCl}_2: \Omega/\text{kJ mol}^{-1} = 9.87 - 15.1y_{\text{CaCl}_2} + 5.44y_{\text{CaCl}_2}^2 \quad (12)$$

NaCl–KCl: $\Omega/\text{kJ mol}^{-1} = -2.05 - 0.272y_{\text{NaCl}}$ (13)

Using these data, parameters L_n^{ij} are obtained as shown in Table 2.

Finally, each Ω_{ij} expressed as Eq. (11) is substituted into Eqs. (8) and (9) under the condition that $y_i - y_j$ is equal to $x_i - x_j$, which is called a Muggianu-type approximation [34].

References

1. Kroll W (1940) The production of ductile titanium. J Electrochem Soc 78:35–47. https://doi.org/10.1149/1.3071290
2. Chen GZ, Fray DJ, Farthing TW (2000) Direct electrochemical reduction of titanium dioxide to titanium in molten calcium chloride. Nature 407:361–364. https://doi.org/10.1038/35030069
3. Ono K, Suzuki RO (2002) A new concept for producing Ti sponge: calciothermic reduction. JOM 54:59–61. https://doi.org/10.1007/BF02701078
4. Crowley G (2003) How to extract low-cost titanium. Adv Mater Process 161:25–27
5. Takeda O, Okabe TH (2006) High-speed titanium production by magnesiothermic reduction of titanium trichloride. Mater Trans 47:1145–1154. https://doi.org/10.2320/matertrans.47.1145
6. Okabe TH, Oda T, Mitsuda Y (2006) Titanium powder production by preform reduction process (PRP). J Alloys Compd 364:156–163. https://doi.org/10.1016/S0925-8388(03)00610-8
7. Zhang Y, Fang ZZ, Xia Y, Huang Z, Lefler H, Zhang T, Sun P, Free ML, Guo J (2016) A novel chemical pathway for energy efficient production of Ti metal from upgraded titanium slag. Chem Eng J 286:517–527. https://doi.org/10.1016/j.cej.2015.10.090
8. Maruyama S, Kado Y, Uda T (2013) Phase diagram investigations of the Bi–Ti system. J Phase Equilib Diffus 34:289–296. https://doi.org/10.1007/s11669-013-0243-0
9. Kado Y, Kishimoto A, Uda T (2015) New smelting process for titanium: magnesiothermic reduction of TiCl$_4$ into liquid Bi and subsequent refining by vacuum distillation. Metall Mater Trans B 46:57–61. https://doi.org/10.1007/s11663-014-0164-2
10. Kishimoto A, Kado Y, Uda T (2016) Electrorefining of titanium from Bi–Ti alloys in molten chlorides for a new smelting process of titanium. J Appl Electrochem 46:987–993. https://doi.org/10.1007/s10800-016-0983-8
11. Kishimoto A, Kuramitsu A, Tsuchihashi K, Uda T (2016) Continuous production of Bi–Ti alloys by magnesiothermic reduction of TiCl$_4$ for a new smelting process of Ti. J MMIJ 123:199–206. https://doi.org/10.2473/journalofmmij.132.199

12. Kishimoto A, Uda T (2018) Thermodynamics on the Bi–Fe–Ti system and the gibbs energy of Bi_9Ti_8. Metall Mater Trans B 49:2975–2985. https://doi.org/10.1007/s11663-018-1393-6

13. Tomonari T (2001) Chitan Kogyo to Sono Tenbo. The Japan Titanium Society, Japan

14. Furihata S, Akashi K, Kurosawa S (1981) The polarographic reduction wave of magnesium ion(II) in a molten LiCl–KCl eutectic mixture. Electrochim Acta 26:1107–1109. https://doi.org/10.1016/0013-4686(81)85085-2

15. Rao GM (1988) Electrochemical studies of magnesium ions in magnesium chloride containing chloride melt at 710 ± 10 °C. J Electroanal Chem 249:191–203. https://doi.org/10.1016/0022-0728(88)80359-0

16. Kisza A, Kaźmierczak J, Børresen B, Haarberg GM, Tunold R (1995) Kinetics and mechanism of the magnesium electrode reaction in molten magnesium chloride. J Appl Electrochem 25:940–946. https://doi.org/10.1007/BF00241588

17. Kisza A, Kaźmierczak J, Børresen B, Haarberg GM, Tunold R (1997) Kinetics and mechanism of the magnesium electrode reaction in molten $MgCl_2$–NaCl binary mixtures. J Electrochem Soc 144:1646–1651. https://doi.org/10.1149/1.1837654

18. Børresen B, Haarberg GM, Tunold R (1997) Electrodeposition of magnesium from halide melts—charge transfer and diffusion kinetics. Electrochim Acta 42:1613–1622. https://doi.org/10.1016/S0013-4686(96)00322-2

19. Martínez AM, Børresen B, Haarberg GM, Castrillejo Y, Tunold R (2004) Electrodeposition of magnesium from $CaCl_2$–NaCl–KCl–$MgCl_2$ melts. J Electrochem Soc 151:C508–C513. https://doi.org/10.1149/1.1758814

20. Moser Z, Krohn C (1974) Thermodynamic properties of liquid magnesium–bismuth alloys. Metall Trans 5:979–985. https://doi.org/10.1007/BF02644308

21. Nayeb-Hashemi AA, Clark JB (1985) The Bi-Mg (bismuth–magnesium) system. Bull Alloys Phase Diag 6:528–533. https://doi.org/10.1007/BF02887150

22. Kosemura S, Ampo S, Fukasawa E, Hatta Y (2007) Production of titanium metal at Toho Titanium Co., Ltd. J MMIJ 123:693–697. https://doi.org/10.2473/journalofmmij.123.693

23. Güden M, Karakaya İ (1994) Electrolysis of $MgCl_2$ with a top inserted anode and an Mg–Pb cathode. J Appl Electrochem 24:791–797. https://doi.org/10.1007/BF00578096

24. Demirci G, Karakaya İ (2007) Collection of magnesium in an Mg–Pb alloy cathode placed at the bottom of the cell in $MgCl_2$ electrolysis. J Alloys Compd 439:237–242. https://doi.org/10.1016/j.jallcom.2006.08.064

25. Leung P, Heck SC, Amietszajew T, Mohamed MR, Conde MB, Dashwood RJ, Bhagat R (2015) Performance and polarization studies of the magnesium–antimony liquid metal battery with the use of *in-situ* reference electrode. RSC Adv 5:83096–83105. https://doi.org/10.1039/c5ra08606j

26. Newhouse JM, Sadoway DR (2017) Charge-transfer kinetics of alloying in Mg-Sb and Li-Bi liquid metal electrodes. J Electrochem Soc 164:A2665–A2669. https://doi.org/10.1149/2.1571712jes

27. Bard AJ (1976) Encyclopedia of electrochemistry of the elements, vol 10. Marcel Dekker Inc, New York

28. Komura A, Imanaga H, Watanabe N (1971) Chlorine evolution process in magnesium chloride–potassium chloride melt. Kogyo Kagaku Zassshi 74:867–871. https://doi.org/10.1246/nikkashi1898.74.5_867

29. The Electrochemical Society of Japan (2000) Denki Kagaku Binran, 5th edn. Maruzen Publishing Co., Ltd, Tokyo

30. Egan JJ, Bracker J (1974) Thermodynamic properties of some binary fused chloride mixtures obtained from e.m.f. measurements. J Chem Thermodyn 6:9–16. https://doi.org/10.1016/0021-9614(74)90201-8

31. Redlich O, Kister AT (1948) Algebraic representation of thermodynamic properties and the classification of solutions. Ind Eng Chem 40:345–348. https://doi.org/10.1021/ie50458a036

32. Papatheodorou GN, Kleppa OJ (1967) Enthalpies of mixing in some binary alkaline-earth chlorides. J Chem Phys 47:2014–2020. https://doi.org/10.1063/1.1712231

33. Hersh LS, Kleppa OJ (1965) Enthalpies of mixing in some binary liquid halide mixtures. J Chem Phys 42:1309–1322. https://doi.org/10.1063/1.1696115

34. Pelton AD (2001) A general "geometric" thermodynamic model for multicomponent solutions. CALPHAD 25:319–328. https://doi.org/10.1016/S0364-5916(01)00052-9

35. Dinsdale AT (1991) SGTE data for pure elements. CALPHAD 15:317–425. https://doi.org/10.1016/0364-5916(91)90030-N

36. Perry GS, Fletcher H (1993) The magnesium chloride–potassium chloride phase diagram. J Phase Equilib 14:172–178. https://doi.org/10.1007/BF02667805

37. Chase NW Jr (1998) NIST-JANAF, thermochemical tables, 4th edn. ACS and AIP, Washington, D. C.